JOURNAL OF COMPUTATIONAL PHYSICS 62, 361–382 (1986)

An Isoparametric Spectral Element Method for Solution of the Navier–Stokes Equations in Complex Geometry

KAROL Z. KORCZAK AND ANTHONY T. PATERA

Department of Mechanical Engineering, Massachusetts Institute of Technology, Cambridge, Massachusetts 02139

Received November 30, 1984; revised March 25, 1985

An isoparametric spectral element technique is presented for solution of the two-dimensional Navier–Stokes equations in arbitrary (curvy) geometries. The spatial discretization is described, and the method is illustrated by solution of Poisson's equation in a cylindrical annulus. A fractional-step Navier–Stokes solver based on a discretely consistent Poisson equation for the pressure is then presented, and exponential convergence in space is demonstrated for the case of (separated) flow between eccentric rotating cylinders. The technique is made efficient by the use of explicit collocation (rather than Galerkin) operators for the convective terms, and use of static condensation to solve the elliptic equations resulting from the Stokes problem. The algorithm is amenable to a high degree of parallelism, in both multiprocessor and vector-pipeline environments.

INTRODUCTION

There has recently been renewed interest in solution of partial differential equations by use of high-order ("*p*-type") finite element methods. Such methods combine the geometric flexibility of standard low-order finite element (or finite volume) techniques [1], with the rapid convergence properties of spectral methods [2]. Various *p*-type schemes for elliptic problems [3–5] have been proposed, all based on variational formulations and high-order elemental polynomial expansions.

Application of *p*-type methods to more complex equations, in particular the passive scalar or Navier–Stokes equations, is complicated not only by the nature of the equations (e.g., hyperbolic contributions), but also by efficiency considerations as regards the solution procedure. We have recently proposed a *p*-type method for the Navier–Stokes equations, a "spectral" element method [5–7], in which these additional complications are addressed. The method differs slightly from standard Galerkin finite element techniques, in that it exploits collocation operators more usually associated with spectral methods.

Briefly summarized, the spectral element discretization proceeds by first breaking up the domain into a series of quadrangular elements, and representing the geometry, velocity, and pressure as tensor-product high-order Lagrangian inter-

0021-9991/86 $3.00

polants through Chebyshev collocation points. The (non-linear) hyperbolic piece of the Navier–Stokes (or passive scalar) equation is then treated explicitly with collocation, while the (linear) elliptic contributions are handled implicitly with variational projection operators. Previous applications of the method have been limited to fluid flow and heat transfer in channels with expansions [5] and grooves [6, 7]; although such geometries are in some sense "complex," they are nevertheless rectilinear and hence not completely general.

In this paper, we present an isoparametric spectral element discretization for solution of flow problems in fully general, curvy geometries. In Section 1 we introduce the isoparametric formulation, and present the solution procedure for second-order elliptic (Helmholtz) equations. The efficiency of the static condensation matrix inversion technique is discussed, and the exponential convergence rate of the method is demonstrated by solution of a model problem. In Section 2, we present a semi-implicit fractional-step method for solution of the Navier–Stokes equations. The Stokes problem is reduced to a sequence of elliptic operators, which are then solved by the methods presented in Section 1. Lastly, in Section 3, we apply our Navier–Stokes solver to two-dimensional flow between rotating eccentric cylinders, as a demonstration of simulation in complex geometry.

1. Isoparametric Formulation for Elliptic Equations

1.1. *Spatial Discretization*

In this section, we consider solution of the Helmholtz equation in two dimensions,

$$\nabla^2 u - \lambda^2 u = f \qquad \text{in } D, \tag{1a}$$

subject to Dirichlet boundary conditions,

$$u = u_B \qquad \text{on } \partial D. \tag{1b}$$

General Neumann or Robin boundary conditions are easily handled by appropriate modifications of the scheme described below, and for simplicity we therefore consider only the Dirichlet case.

The spatial discretization proceeds by first covering the domain D with general (non-rectilinear) quadrangles, as shown in Fig. 1. Each quadrangle is then mapped from the physical (x, y) space into the local (r, s) co-ordinate system by an isoparametric tensor-product mapping,

$$(x, y)_N^k = \sum_{i=0}^{N} \sum_{j=0}^{N} (X, Y)_{ij}^k h_i(r)\, h_j(s). \tag{2}$$

(Hereafter, unless otherwise noted, all subscripts are taken to run from 0 to N, and summation over repeated indices is assumed unless the pointwise collocation

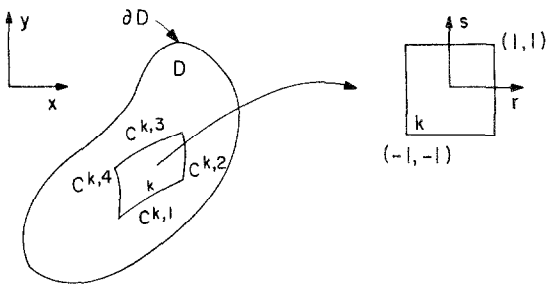

FIG. 1. Isoparametric mapping of element k (sides $C^{k,q}$, $q = 1,..., 4$) from the physical domain (x, y) to the local (r, s) co-ordinate system. The computational domain is denoted D, with boundary ∂D.

product (e.g., $a_q \circ b_q$) is indicated.) Here the $(X, Y)_{ij}^k$ are the physical (x, y) co-ordinates of the grid point mapped to $(r = z_i, s = z_j)$ in element k, and the $h_m(z)$ are Nth order local Lagrangian interpolants,

$$h_m(z_n) = \delta_{mn}, \tag{3}$$

where δ_{pq} is the Kronecker-delta symbol. As per the isoparametric recipe, geometry and data are interpolated in the same fashion, that is,

$$u_N^k(r, s) = u_{ij}^k h_i(r)\, h_j(s), \tag{4a}$$

$$f_N^k(r, s) = f_{ij}^k h_i(r)\, h_j(s). \tag{4b}$$

(For convenience we have chosen the resolution in the two spatial directions to be the same, however, in practice, this need not be the case.) Note the above construction ensures that both the mapping and the interpolant are C^0, a requirement for the variational formulation to be presented below.

To complete the spatial description, the local and physical collocation points, z_n and $(X, Y)_{ij}^k$, respectively, must be specified. For the z_n, we have chosen the Gauss–Lobatto Chebyshev points [5],

$$z_n = -\cos\frac{\pi n}{N}, \tag{5}$$

from which it follows that the interpolants in (3) can be written as

$$h_m(z) = \mu_{mn} T_n(z), \tag{6a}$$

$$\mu_{mn} = \frac{2}{N}\frac{1}{\bar{c}_m \bar{c}_n} T_n(z_m). \tag{6b}$$

Here the T_n are the Chebyshev polynomials,

$$T_n(\cos\theta) = \cos n\theta, \tag{7a}$$

and

$$\begin{aligned} \bar{c}_m &= 1, \qquad m \neq 0, N \\ &= 2, \qquad m = 0, N. \end{aligned} \tag{7b}$$

To determine the physical mesh, $(X, Y)_{ij}^k$, we first specify the $(X, Y)_{ij}^k$ along elemental boundary curves $C^{k,m}$ $(m = 1,..., 4)$ according to a Chebyshev distribution in arclength. On physical boundaries (i.e., where $C^{k,m} \cap \partial D = C^{k,m}$), we assume that the $C^{k,m}$ are given (effectively) exactly. For "internal" elemental boundaries (i.e., for which $C^{k,m} \cap \partial D$ is at most a point), various choices of $C^{k,m}$ are possible; the effect of zoning on the solution accuracy will be discussed in the context of the model problem solved below. Once the $(X, Y)_{ij}^k$ are known on all elemental boundaries, the remaining (elemental interior) points are determined by deforming the (r, s) mesh into its (x, y) image using "uniform strain" [8].

The starting point for the finite element method is the equivalence of the differential equation (1a) with maximization of the functional,

$$I(u) = \int \int_D \left[-\frac{1}{2} \nabla u \cdot \nabla u - \frac{\lambda^2}{2} u^2 - uf \right] d\mathbf{x}, \tag{8}$$

with restriction to admissible variations associated with the essential boundary conditions (1b). In element k the functional in local co-ordinates can be written as

$$I^k(u) = \int_{-1}^{1} \int_{-1}^{1} \left[\frac{-\tilde{\nabla} u \cdot \tilde{\nabla} u}{2 |J|} - \frac{|J| \lambda^2 u^2}{2} - |J| uf \right] dr\, ds, \tag{9}$$

where

$$\tilde{\nabla} = \left(-\frac{\partial}{\partial r} y_s + \frac{\partial}{\partial s} y_r \right) \hat{x} + \left(\frac{\partial}{\partial r} x_s - \frac{\partial}{\partial s} x_r \right) \hat{y}, \tag{10}$$

and

$$J = x_s y_r - x_r y_s. \tag{11}$$

(Here subscript r (s) refers to differentiation.)

To get the discretized equations, we first define the discrete values of the geometric transformation factors,

$$(x_s)_{pq} = X_{pm} D_{mq}, \qquad (y_r)_{pq} = Y_{mq} D_{mp}, \ldots \tag{12a}$$

$$J_{pq} = (x_s)_{pq} \circ (y_r)_{pq} - (x_r)_{pq} \circ (y_s)_{pq}, \tag{12b}$$

where $\circ$ indicates the physical space (collocation) product, and D is the derivative matrix,

$$D_{pq} = \frac{dh_p}{dz}(z_q). \tag{13}$$

We now insert the interpolants (4) and geometric transformations (12) into the functional (9), perform the resulting integrals (the choice of quadrature is discussed below), and require stationarity with respect to variations in the u_{ij}^k. This gives the elemental equations

$$C_{ijmn}^k u_{mn}^k = \overset{+}{B}{}_{ijmn}^k f_{mn}^k, \tag{14a}$$

where

$$C_{ijmn}^k = A_{ijmn}^k - \lambda^2 \overset{+}{B}{}_{ijmn}^k, \tag{14b}$$

and

$$A_{ijmn}^k = -\tilde{\nabla}_{pqij}^k \cdot \bar{B}_{pqrs}^k \tilde{\nabla}_{rsmn}^k \tag{15a}$$

$$\overset{\pm}{B}{}_{ijmn}^k = |J_{pq}^k|^{\pm 1} \mathscr{B}_{pim} \mathscr{B}_{qjn} \tag{15b}$$

$$\tilde{B}_{ijmn}^k = \operatorname{sgn}(J_{\cdot\cdot}^k) \mathscr{B}'_{im} \mathscr{B}'_{jn}. \tag{15c}$$

(We introduce the "modified" mass matrix, $\tilde{B}_{ijmn}^k$, now for convenience, although it will not be used until the next section.)

Here $\operatorname{sgn}(J_{\cdot\cdot}^k)$ is the algebraic sign of the Jacobian, which, since J_{ij}^k must be one-signed in a given element, can be evaluated at any node. Also,

$$\begin{aligned}\tilde{\nabla}_{ijmn}^k = {} & (D_{mi} \circ (-y_s)_{mj} \delta_{nj} + D_{nj} \circ (y_r)_{in} \delta_{im}) \hat{x} \\ & + (D_{mi} \circ (x_s)_{mj} \delta_{nj} + D_{nj} \circ (-x_r)_{in} \delta_{im}) \hat{y},\end{aligned} \tag{16}$$

and

$$\mathscr{B}_{ijk} = \int_{-1}^{1} h_i(z)\, h_j(z)\, h_k(z)\, dz \tag{17a}$$

$$= \mu_{il} \mu_{jm} \mu_{kn} b_{lmn}$$

$$\mathscr{B}'_{jk} = \sum_i \mathscr{B}_{ijk}, \tag{17b}$$

where

$$\begin{aligned} b_{lmn} &= \int_{-1}^{1} T_l(z)\, T_m(z)\, T_n(z)\, dz \\ &= \begin{cases} 0, & l+m+n \text{ odd} \\ \dfrac{1}{2}\left[\dfrac{1}{1-(l-n-m)^2} + \dfrac{1}{1-(l+n+m)^2}\right. & \\ \qquad \left. + \dfrac{1}{1-(l-n+m)^2} + \dfrac{1}{1-(l+n-m)^2}\right], & l+m+n \text{ even.} \end{cases} \end{aligned} \tag{18}$$

With respect to efficiency of the elemental matrix set-up, we note that in practice we are interested in time-dependent problems in fixed geometry, for which the matrix construction need only be done once. The above calculations, appropriately factorized, take $O(N^5)$, which appears reasonable for our applications. If required, the process could be made more efficient by use of orthogonality [9].

Once the elemental matrices have been formed, the system matrix is constructed by standard direct stiffness summation, denoted

$$\{C\} = \sum_k{}' [C^k], \tag{19}$$

where $\{\cdot\}$ and $[\cdot]$ refer to global and elemental quantities, respectively. As our elements are C^0, nothing further is required at elemental interfaces. The complete problem statement then becomes,

$$\{C\}\{u\} = \sum_k{}' [\overset{+}{B}{}^k][f^k], \tag{20}$$

where Dirichlet boundary conditions are imposed by eliminating the known degrees-of-freedom (and corresponding rows and columns) from the system equations.

1.2. *Matrix Inversion by Static Condensation*

The technique described above, however accurate, is of little practical interest unless the resulting equations, (20), can be efficiently solved. In particular, the use of high-order elements introduces long-range coupling and associated large bandwidths in the system matrices. However, at least on parallel processors, a solution algorithm can be easily constructed for the spectral element equations that gives an operation count competitive with that for a low order finite element solution with commensurate degrees-of-freedom (and, presumably, lower accuracy). In particular, we apply standard static condensation [10], grouping the nodes and corresponding degrees-of-freedom into those lying on elemental boundaries, and those interior to an element, $[{}^B u^k]$ and $[{}^I u^k]$, respectively.

In terms of this decomposition, the elemental equations can be written in block form as

$$[a^k][{}^B u^k] + [b^k]^T[{}^I u^k] = [{}^B g^k] \tag{21a}$$

$$[b^k][{}^B u^k] + [c^k][{}^I u^k] = [{}^I g^k], \tag{21b}$$

where $[g^k] = [B^k][f^k]$. Solving for $[{}^I u^k]$ in (21b) and inserting this into equation (21a) gives

$$[\tilde{a}^k][{}^B u^k] = [{}^B \tilde{g}^k] \tag{22a}$$

$$[c^k][{}^I u^k] = [{}^I g^k] - [b^k][{}^B u^k], \tag{22b}$$

where

$$[\hat{a}^k] = [a^k] - [b^k]^T [c^k]^{-1} [b^k], \tag{23a}$$

$$[{}^B\hat{g}^k] = [{}^Bg^k] - [b^k]^T [c^k]^{-1} [{}^Ig^k]. \tag{23b}$$

The key to the method's efficiency is that all coupling (by direct stiffness) between elements involves only the equations for the $[{}^Bu^k]$. Thus, we can first solve for the $[{}^Bu^k]$ by inverting the condensed system,

$$\{\hat{a}\}\{{}^Bu\} = \{{}^B\hat{g}\} \tag{24}$$

(which is of greatly reduced rank compared to the original system (20)), and then perform all the elemental calculations (22b) for the $[{}^Iu^k]$ (which constitute the majority of the degrees-of-freedom for a high-order method) *in parallel.* (Note that, in practice, only elemental boundary nodes need be ascribed global specifiers, as all other operations are local to a given element.)

Our interest in the solution of elliptic equations is in the context of time-dependent Navier–Stokes simulations, as described in the following sections of this paper. In particular, a splitting algorithm will be given that reduces the Stokes problem to a series of (time-independent coefficient) elliptic problems. We therefore do the $\mathrm{LDL}^{\mathrm{T}}$ decomposition of (24) and form the $[c^k]^{-1}$ required by (22b) once at the beginning of the simulation, and thereafter do only the requisite forward- and back-solves and matrix multiplies at each time step. For a system of M by M elements, each with N by N degrees-of-freedom, the operation count/time step (assuming for simplicity M^2 processors) for the $[{}^Iu^k]$ is $O(N^4)$. For the solves in (24), the count is approximately $O(M^3N^2)$ (assuming no parallelism) using the $\mathrm{LDL}^{\mathrm{T}}$ decomposition.

Although the $\mathrm{LDL}^{\mathrm{T}}$ decomposition is the obvious choice for solution of (24) on a serial processor, we have found that, due to the comparatively few degrees-of-freedom in $[{}^Bu^k]$, and the relatively large bandwith of $\{\hat{a}\}$, formation of the full inverse $\{\hat{a}\}^{-1}$ is often more efficient on a vector processor (e.g., the CRAY-1). Furthermore, the full inverse is trivially broken up on a parallel processor, with a minimum of communication between processors. Indeed, on our hypothetical M^2-headed machine, the operation count for solution of (24) using the full inverse would be $O(M^2N^2)$, fully vectorized.

It is interesting to note that, if parallel static condensation were applied to a low-order finite element solver based on substructures [10] similar (in extent and number of grid points) to corresponding spectral elements, the operation count for finding the $[{}^Bu^k]$ would be roughly the same as for our high-order method. The reason for this is that $[\hat{a}^k]$ must be formed in (23) via $[c^k]^{-1}$, which will be full even for low-order (sparse) approximations. Note this comparison between high- and low-order techniques is valid only for this particular algorithm (static condensation), and does not imply that other possible approaches for exploiting parallelism in low order methods will not give these techniques a lower operation

count. However, parallel static condensation is nevertheless attractive, in that it represents an implicit algorithm with natural, easily implemented concurrency, and a minimum of interelemental communication.

1.3. *Convergence Rate of the Method*

We discuss the accuracy of the spectral element method as applied to second-order elliptic problems with smooth solutions, and consider the case where the solution converges as the order of (a fixed number of) elements is increased. Although we do not attempt to derive a rigorous error bound, it is clear that there will be three contributions to such an estimate [1]. First, there is the error due to the fact that the (assumed exact) functional is minimized in a restricted subspace of $\mathscr{H}^1$ [1] rather than over the entire space. Second, there is the error due to the fact that inhomogeneous terms in the functional, for instance, $u_N^k f^k$, are not integrated exactly; rather, we interpolate $f^k \to f_N^k$, and then perform an exact quadrature of $u_N^k f_N^k$. Note that for solution of time-dependent partial differential equations (that is, where marching is appropriate), the inhomogeneities are typically related to the solution at earlier times, in which case integration of the interpolant is the best quadrature available. Third, there is the error due to perturbation of the functional by inexact representation and integration of the geometric transformation factors (12). This source of error, unlike that due to inhomogeneities such as f, could be made arbitrarily small by choice of a quadrature rule of sufficiently high order. The particular discretization given in (14)–(15) is appropriate for the Stokes solver to be discussed below, however, other choices are certainly possible.

The first error in no way depends on the choice of collocation points, as these only effect the representation of the subspace, i.e., the basis. This error can be estimated in terms of the best fit of the solution, u, by our polynomial space [1]. In contrast, the second and third errors depend strongly on the choice of collocation points, and it would appear that these errors can be bounded by the error incurred in interpolation (by the *particular* basis chosen) of geometry and data. Our choice of Chebyshev in arclength for $(X, Y)_{ij}^k$, and Chebyshev for the local collocation points z_n, seems a reasonable solution to the interpolation problem, given the exponential convergence of Chebyshev representation of infinitely smooth functions [11]. In fact, we would expect that, for problems with smooth solutions, the spectral element method will converge at least exponentially as the order of the elements is increased.

It is important to note that, although we use Chebyshev interpolation, the technique is not a Chebyshev spectral technique [2], in the sense that we use the unity rather than $(1-z^2)^{-1/2}$ weighting in (8). It is for this reason that most of the standard theoretical estimates concerning finite element solution of elliptic equations should apply, with appropriate modification of interpolation and approximation results. (The unity weighting would in fact suggest a Legendre basis as more natural; little modification of the above formulation is required to effect this change.)

Empirical studies [5] in rectilinear geometry indicate that, for sufficiently smooth solutions, the method does in fact give exponentially convergent results. We "demonstrate" that this rapid convergence is maintained for the full isoparametric formulation in curvy geometries, by considering the Poisson equation

$$\nabla^2 u = \sin\theta \left\{ \frac{2\pi}{r} \cos 2\pi(r-1) - \left[\frac{1}{r^2} + (2\pi)^2 \right] \sin 2\pi(r-1) \right\}, \tag{25a}$$

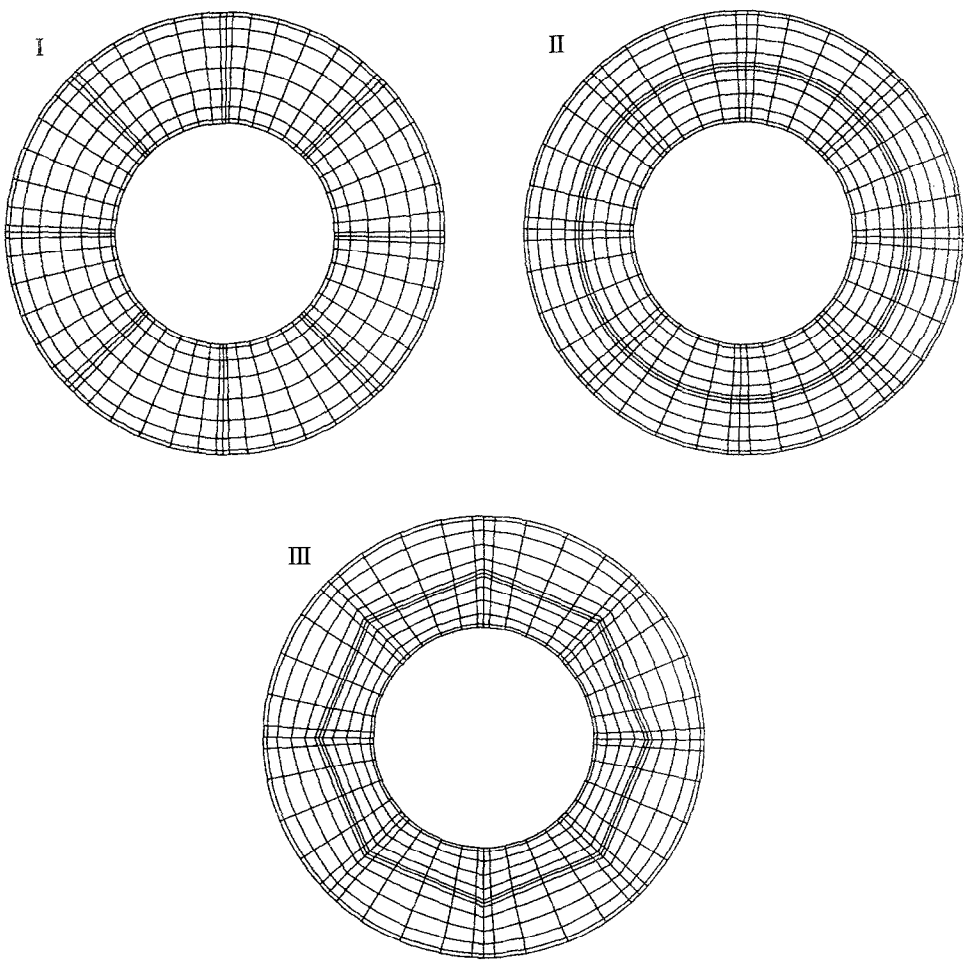

FIG. 2. Spectral element meshes used for solution of Poisson's equation in an annulus. Mesh I is essentially spectral in r, while Meshes II and III have two elements ($M_r = 2$) in the radial direction. For Meshes II and III the interelemental (radial) boundary C_B is given by a circular arc and straight line, respectively. All meshes have eight elements in the azimuthal direction.

in the annulus $1 \leqslant r \leqslant 2$, $0 \leqslant \theta \leqslant 2\pi$, with boundary conditions $u(r=1, \theta)=1$, $u(r=2, \theta)=0$. The solution to this problem is

$$u = 1 - \frac{\ln r}{\ln 2} + \sin\theta \sin 2\pi(r-1). \tag{25b}$$

Clearly the best way to solve this problem would be to use a Fourier method in θ, which would result in a one-dimensional problem in r. However, to test our method, we consider the series of meshes shown in Fig. 2. These meshes are characterized by the number of elements in the r direction, M_r (here $M_r = 1$ or 2), and, for $M_r = 2$, the (analytical) description of the common internal boundary between elements, C_B. In the azimuthal direction, all meshes have eight elements, and the internal boundaries are always taken to be straight lines. Mesh I has $M_r = 1$, and is essentially spectral in r. Meshes II and III have $M_r = 2$, with C_B given by a circular arc and straight line, respectively.

In Fig. 3 we plot the maximum pointwise error over all grid-points (the dependency of the true L_∞-norm is similar) for the various solutions (I–III) as a function of number of degrees-of-freedom. All meshes are seen to give exponentially convergent solutions, and for this particular problem, roughly the same accuracy. Note for problems which demand high resolution in the interior of a domain, elemental approaches are typically *more* accurate than global methods [12], as nodes can be concentrated near regions of rapid variation.

It is clear that the exponential convergence rate demonstrated here will not

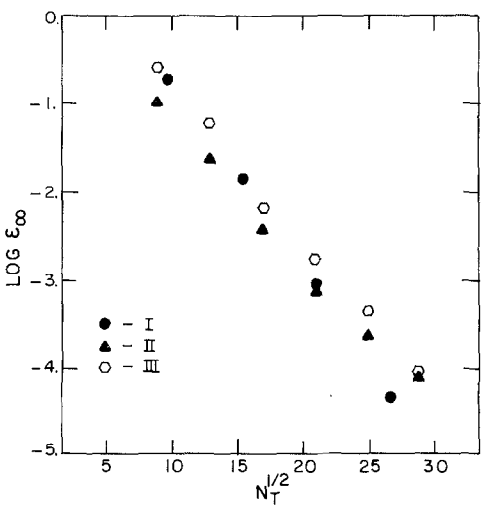

FIG. 3. A plot of the L_∞-error in the solution to Poisson's equation in an annulus, as a function of $N_T^{1/2}$, where N_T is the total number of nodes in the mesh. Note the three meshes give roughly the same accuracy, and all demonstrate exponential convergence.

obtain when singularities induced by geometry (e.g., corners) or boundary data are present. In such cases, unless special refinement [4] or subtraction [1] techniques are employed, the convergence rate will only be finite-order [3].

2. Time-Splitting Scheme for the Navier–Stokes Equations

2.1. *Semi-Discrete Equations*

The incompressible Navier–Stokes equations, written in rotational form, are

$$\frac{\partial \mathbf{v}}{\partial t} = \mathbf{v} \times \boldsymbol{\omega} - \nabla \Pi + \nu \nabla^2 \mathbf{v} + \mathbf{f} \qquad \text{in } D \tag{26a}$$

$$\nabla \cdot \mathbf{v} = 0 \qquad \text{in } D, \tag{26b}$$

where (26a) is the momentum equation, and (26b) corresponds to mass conservation. Here $\mathbf{v}(\mathbf{x}, t)$ $(= u\hat{x} + v\hat{y})$ is the velocity, $\boldsymbol{\omega}$ is the vorticity, $\boldsymbol{\omega} = \nabla \times \mathbf{v}$, Π is the dynamic pressure, $\Pi = p + \frac{1}{2}\mathbf{v} \cdot \mathbf{v}$, and $\mathbf{f}$ is the prescribed force. We assume that the equations have been appropriately non-dimensionalized so that ν is the inverse Reynolds number, and the density is unity. In addition to (26), we require no-slip boundary conditions

$$\mathbf{v} = \mathbf{v}_w \qquad \text{on } \partial D, \tag{27a}$$

and initial conditions,

$$\mathbf{v}(\mathbf{x}, t = 0) = \mathbf{v}_0(\mathbf{x}) \qquad \text{in } D. \tag{27b}$$

For problems with unbounded domains, (27a) must be replaced with appropriate inflow/outflow or periodic conditions. As our interest here is not the inflow/outflow problem, we restrict ourselves to the case where $\mathbf{v}_w \cdot \hat{n} = 0$ on all (non-periodic) boundaries, where $\hat{n}$ is the outward normal on ∂D.

Before considering the fully-discrete case, we consider the semi-discrete (in time) version of the splitting scheme [13] to be used. The non-linear terms are treated explicitly using third-order Adams–Bashforth,

$$\frac{\hat{\mathbf{v}}^{n+1} - \mathbf{v}^n}{\Delta t} = \frac{23}{12}(\mathbf{v} \times \boldsymbol{\omega} + \mathbf{f})^n - \frac{16}{12}(\mathbf{v} \times \boldsymbol{\omega} + \mathbf{f})^{n-1} + \frac{5}{12}(\mathbf{v} \times \boldsymbol{\omega} + \mathbf{f})^{n-2}, \tag{28}$$

the third-order scheme being chosen for its relatively large stability region near the imaginary axis [14]. Note no boundary conditions are imposed at this step. Once

$\hat{\mathbf{v}}^{n+1}$ is calculated, we are left with an unsteady Stokes problem, which is split in time. First there is the pressure step,

$$\frac{\hat{\hat{\mathbf{v}}}^{n+1} - \hat{\mathbf{v}}^{n+1}}{\Delta t} = -\nabla \Pi \qquad \text{in } D \tag{29a}$$

$$\nabla \cdot \hat{\hat{\mathbf{v}}}^{n+1} = 0 \qquad \text{in } D \tag{29b}$$

$$\hat{\hat{\mathbf{v}}} \cdot \hat{n} = \mathbf{v}_w \cdot \hat{n} = 0 \qquad \text{on } \partial D, \tag{29c}$$

which can also be formulated as

$$\nabla^2 \Pi = \nabla \cdot \left(\frac{\hat{\mathbf{v}}^{n+1}}{\Delta t} \right) \qquad \text{in } D \tag{30a}$$

$$\frac{\hat{\hat{\mathbf{v}}}^{n+1} - \hat{\mathbf{v}}^{n}}{\Delta t} = -\nabla \Pi \qquad \text{in } D \tag{30b}$$

$$\frac{\partial \Pi}{\partial n} = \frac{\hat{\mathbf{v}}^{n+1} \cdot \hat{n}}{\Delta t} \qquad \text{on } \partial D. \tag{30c}$$

This is then followed by the viscous step,

$$\left(\nabla^2 - \frac{2}{\nu \Delta t} \right) (\mathbf{v}^{n+1} + \mathbf{v}^n) = \frac{-2}{\nu \Delta t} (\hat{\hat{\mathbf{v}}}^{n+1} + \mathbf{v}^n) \qquad \text{in } D \tag{31a}$$

$$\mathbf{v}^{n+1} = \mathbf{v}_w. \qquad \text{on } \partial D. \tag{31b}$$

Although the above scheme uses the improper (inviscid) boundary condition on the pressure, it has been shown (at least for model problems) [15] that the method

walls. The scheme can also be thought of as a time-accurate artificial compressibility method with $1/\Delta t$ as the penalty parameter. The accuracy can be improved to $O(\Delta t^2)$ everywhere by use of Green's function techniques [5] or iterative procedures [15]. However, at least at high Reynolds number (where $\nu \Delta t$ is typically small), the splitting scheme achieves comparable accuracy to these higher-order methods, with considerably less work and complexity. We make no further excuses for the method, and indicate how it can be implemented for complex geometries in the context of the spectral element spatial discretization.

2.2. *Fully-Discrete Equations*

We consider here the fully-discrete algorithm for two-dimensional flow; the method formally extends to the three-dimensional case, trivially so if a Fourier spectral method is used in the third direction [7]. The basic spatial discretization is

similar to that for the Helmholtz equation discussed in Section 1. In particular, the velocity and pressure are interpolated on the same mesh (i.e., with the same basis),

$$\mathbf{v}_N^k(r, s) = \mathbf{v}_{ij}^k h_i(r)\, h_j(s) \tag{32a}$$

$$\Pi_N^k(r, s) = \Pi_{ij}^k h_i(r)\, h_j(s), \tag{32b}$$

contrary to standard finite element theory, which typically requires a lower-order interpolant for the pressure [16].

For the nonlinear step, standard collocation is used [2],

$$\frac{\hat{\mathbf{v}}_{ij}^{k,n+1} - \mathbf{v}_{ij}^{k,n}}{\Delta t} = \frac{23}{12}(\mathbf{v}_{ij}^k \times \boldsymbol{\omega}_{ij}^k + \mathbf{f}_{ij}^k)^n - \frac{16}{12}(\mathbf{v}_{ij}^k \times \boldsymbol{\omega}_{ij}^k + \mathbf{f}_{ij}^k)^{n-1} + \frac{5}{12}(\mathbf{v}_{ij}^k \times \boldsymbol{\omega}_{ij}^k + \mathbf{f}_{ij}^k)^{n-2}, \tag{33a}$$

where the vorticity is given by

$$\boldsymbol{\omega}_{ij}^k = \hat{z}\, \frac{1}{J_{ij}^k} \circ \tilde{\nabla}_{ijmn}^k \times \mathbf{v}_{mn}^k, \tag{33b}$$

and $\hat{z}$ is the unit vector out of the plane of motion. No boundary conditions are imposed on this step, however the intermediate velocity, $\hat{\mathbf{v}}$, is averaged at element interfaces so that the final result is continuous across the flow domain. It is critical for the efficiency of the scheme that collocation be used for the non-linear terms, as the convolution sums required by the Galerkin formulation are prohibitively costly to evaluate when high-order expansions are used [2].

We then take the inviscid pressure step (corresponding to (30)),

$$\Delta t \sum_k{}' A_{ijmn}^k \Pi_{mn}^k = \sum_k{}' -\tilde{\nabla}_{pqij}^k \cdot \tilde{B}_{pqmn}^k \hat{\mathbf{v}}_{mn}^{k,n+1} \tag{34a}$$

$$\sum_k{}' \tilde{B}_{pqmn}^k (\hat{\mathbf{v}}_{mn}^{k,n+1} - \hat{\mathbf{v}}_{mn}^{k,n+1}) = -\Delta t \sum_k{}' \bar{B}_{pqrs}^k \tilde{\nabla}_{rsmn}^k \Pi_{mn}, \tag{34b}$$

followed by the viscous correction,

$$\sum_k{}' C_{ijmn}^k (\mathbf{v}_{mn}^{k,n+1} + \mathbf{v}_{mn}^{k,n}) = \frac{-2}{\nu\, \Delta t} \sum_k{}' \overset{+}{B}{}_{ijmn}^k (\hat{\mathbf{v}}_{mn}^{k,n+1} + \mathbf{v}_{mn}^{k,n}) \qquad \text{in } D \tag{35a}$$

$$\mathbf{v}_{ij}^{k,n+1} = \mathbf{v}_w(X_{ij}^k,\ Y_{ij}^k) \qquad \text{on } \partial D, \tag{35b}$$

where

$$C_{ijmn}^k = A_{ijmn}^k - \frac{2}{\nu\, \Delta t} \overset{+}{B}{}_{ijmn}^k. \tag{36}$$

The Dirichlet conditions in (35b) are imposed by eliminating the boundary degrees-of-freedom from the system matrix. The elliptic operators in (34) and (35) are inverted using the static condensation algorithm discussed in Section 1.

2.3. *Incompressibility Condition*

In this section, we discuss the form of the pressure Poisson equation in (34a). We analyze in what sense it imposes incompressibility, demonstrate that it automatically incorporates the necessary boundary conditions, (30c), and show that the discrete equations, although singular, are always solvable. For this purpose, it is useful to view (34a) not only as a discrete analog of the continuous system, (30a), but also as a "consistent" Poisson equation derived from a discrete incompressibility constraint [17, 18]. In particular, (34a) can be obtained from the following discrete versions of (29a) and (29b),

$$\tilde{B}^k_{pqmn}(\hat{\mathbf{v}}^{k,n+1}_{mn} - \hat{\mathbf{v}}^{k,n+1}_{mn}) = -\Delta t\, \bar{B}^k_{pqrs} \tilde{\nabla}^k_{rsmn} \Pi^k_{mn} \tag{37a}$$

and

$$\sum_k{}' - \tilde{\nabla}^k_{pqij} \cdot \tilde{B}^k_{pqmn} \hat{\mathbf{v}}^{k,n+1}_{mn} = 0, \tag{37b}$$

respectively, by operating on (37a) with the transpose gradient operator, $\tilde{\nabla}^k_{pqij}(\cdot)$, performing direct stiffness, and utilizing the condition (37b). Note that (34) and (37) are, in fact, not equivalent, as (37a) is elemental, whereas (34b) is global. We discuss this distinction further below.

The weak sense in which the above system imposes the divergence-free condition (and, in fact, the sense in which the right-hand side of (34a) corresponds to the divergence in (30a)) can be better seen by using the interpolation identity,

$$\frac{dh_i}{dz}(z) \equiv D_{im} h_m(z), \tag{38}$$

and integration by parts, to rewrite the elemental components of (37b) as

$$-\tilde{\nabla}^k_{pqij} \cdot \tilde{B}^k_{pqmn} \hat{\mathbf{v}}^{k,n+1}_{mn} = \mathscr{D}^k_{ij} + \mathscr{F}^k_{ij}, \tag{39a}$$

where (dropping the time-level and element superscripts),

$$\begin{aligned} \mathscr{D}^k_{ij} = &-(y_s)_{ij} \circ \tilde{B}_{ijmn}(\hat{u}_r)_{mn} + (x_s)_{ij} \circ \tilde{B}_{ijmn}(\hat{v}_r)_{mn} \\ &+ (y_r)_{ij} \circ \tilde{B}_{ijmn}(\hat{u}_s)_{mn} - (x_r)_{ij} \circ \tilde{B}_{ijmn}(\hat{v}_s)_{mn}, \end{aligned} \tag{39b}$$

$$\mathscr{F}^k_{ij} = \sum_{q=1}^{4} \mathscr{F}^{k,q}_{ij}; \quad \mathscr{F}^{k,q}_{(m;q)} = -\operatorname{sgn}(J^k)\, \sigma_q \{(-y_z)_{(m;q)} \circ \mathscr{B}'_{mn} \hat{u}(n;q) + (x_z)_{(m;q)} \circ \mathscr{B}'_{mn} \hat{v}(n;q)\}, \tag{39c}$$

(with $\mathscr{F}_{ij}^{k,q}=0$ at all nodes *not* on sides $C^{k,q}$). Here $\sigma_q=1$, (-1) for $q=1, 2(3, 4)$, $(m; q)$ refers to the sets of nodes $(m, 0)$, (N, m), (m, N), and $(0, m)$ for $C^{k,q}q=1,..., 4$, respectively, and $z=r(s)$ along sides $C^{k,q}$ with $q=1, 3(2, 4)$.

If we now *assume* C^0-continuity of the solution $\hat{\hat{\mathbf{v}}}$ the flux terms $\mathscr{F}_{ij}^{k}$ cancel at all internal elemental boundaries upon direct stiffness summation, and (37b) is therefore found to be equivalent to

$$\sum_k{}' \mathscr{D}_{ij}^{k}=0 \qquad \text{in } D \tag{40a}$$

$$\sum_k{}' (\mathscr{D}_{ij}^{k}+\mathscr{F}_{ij}^{k})=0 \qquad \text{on } \partial D. \tag{40b}$$

Thus, at all internal "points," the divergence is zero in the weighted sense of (40a). At points on physical boundaries, there is an additional term corresponding to mass flow into the domain, (40b); however, this mass flow will be on the order of the discretization error. This can be seen by applying the identity (39) to $\hat{\mathbf{v}}$, and recognizing that the boundary condition imposed on Π in (34a) is therefore $\partial\Pi/\partial n=\hat{\mathbf{v}}\cdot\hat{n}/\Delta t$ (implying $\hat{\hat{\mathbf{v}}}\cdot\hat{n}=0$). The Neumann condition in the continuous case, (30c), reappears automatically in the discrete equation, (34a), as a natural boundary condition.

In arriving at the above conclusions, we assumed that $\hat{\hat{\mathbf{v}}}$ would be continuous across elemental boundaries. However, this will not be the case from (37a), as only C^0-continuity is required of the pressure in (32b), implying a discontinuous pressure gradient at elemental boundaries. As a result, the right-hand-sides in (40) are, in fact, not zero, but order the discretization error. In some sense, we only "naturally" impose the divergence-free condition, and thus, strictly speaking, the Poisson equation for the pressure, (34a), is not "consistent" with (37b). In practice, we of course solve (34), not (37), for reasons of computational efficiency.

As in all incompressible flows, the pressure is only determined to within a constant. As a result, one must be certain that the Poisson equation for the pressure is, in fact, solvable. In particular, although the semi-discrete formulation is trivially compatible,

$$\int_D \nabla^2\Pi\, d\mathscr{V}=\int_{\partial D}\frac{\partial\Pi}{\partial n}\,dS=\int_{\partial D}\frac{\hat{\mathbf{v}}^{n+1}\cdot\hat{n}}{\Delta t}\,dS=\int_D \nabla\cdot\left(\frac{\hat{\mathbf{v}}^{n+1}}{\Delta t}\right)d\mathscr{V}, \tag{41}$$

this must also obtain for the discrete Poisson system (34a). It is simple to show that this is, indeed, the case, by noting that for the transpose gradient operator,

$$\sum_{ij}\tilde{\nabla}_{pqij}^{k}=(-D_{ip}Y_{im}D_{mq}+D_{jq}Y_{mj}D_{mp})\,\hat{x} + (D_{ip}X_{im}D_{mq}-D_{jq}X_{mj}D_{mp})\,\hat{y}=0. \tag{42}$$

This relation implies that the right-hand side of (34a) is orthogonal to the (unity) left nullspace of the Poisson operator, and the system is therefore solvable.

It is clear from the construction of the Laplace operator (15a) that appears in the Poisson equation for the pressure (34a), that there is only the one ("hydrostatic") mode in the nullspace of this discrete system. This is in contrast to, but not in variance with, the fact that most finite element schemes (in particular, methods using equal order interpolants for pressure and velocity) exhibit additional spurious "chequerboard" modes [19] in the pressure. The reason these do not appear here is due to the weak requirement on the divergence (40), and, more specifically, the fact that this condition is only "naturally" imposed. Also, these spurious modes are strongly affected by the boundary conditions on velocity [19, 20], and our conditions on $\hat{\hat{\mathbf{v}}}$ are quite weak (corresponding to natural imposition of (29c)). Note our discussion of the discrete incompressibility condition is only in the context of the Euler problem; our splitting scheme for the Stokes problem results in significant "error" in the boundary divergence at the end of the full step (35).

The success of the pressure step is primarily due to use of the transpose gradient operator (in conservative form), and the fact that the Jacobian terms can be explicitly cancelled in weighted residual formulations of divergence inhomogeneities (hence the modified mass matrix, $\tilde{B}^k_{pqmn}$, in (34b)). The latter can also be exploited to construct schemes for non-linear and linear convective equations using mixed collocation/Galerkin methods, in which the efficiency of the former is combined with the conservation properties of the latter [12, 21].

The formal procedure we have described here for the pressure requires solution of the Poisson equation (34a), followed by an additional matrix inversion in (34b) to determine the velocities. We have found empirically that the Galerkin formulation in (34b) can be replaced by collocation with minimal effect,

$$\frac{\hat{\hat{\mathbf{v}}}^{k,n+1}_{ij} - \hat{\mathbf{v}}^{k,n+1}_{ij}}{\Delta t} = -\frac{1}{J^k_{ij}} \circ \tilde{\nabla}^k_{ijmn} \Pi^k_{mn}, \tag{43a}$$

thereby eliminating the matrix inversion. Another alternative is to re-formulate the Galerkin problem (34b) as

$$\sum_k{}' \overset{+}{B}{}^k_{pqmn} (\hat{\hat{\mathbf{v}}}^{k,n+1}_{mn} - \hat{\mathbf{v}}^{k,n+1}_{mn}) = -\Delta t \sum_k{}' \tilde{B}^k_{pqrs} \tilde{\nabla}^k_{rsmn} \Pi_{mn}. \tag{43b}$$

In this case no matrix inversion is required, as it is the left-hand-side of (43b) required in the viscous step (35a).

3. Flow between Eccentric Rotating Cylinders

In this section, we demonstrate empirically that our Stokes solver is, indeed, $O(\Delta t)$ accurate in time, exponentially-convergent in space, as might be expected

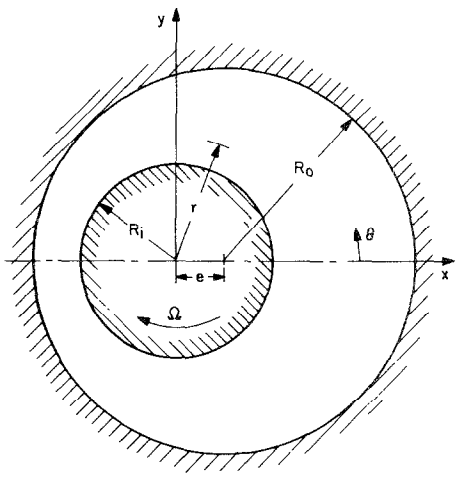

FIG. 4. Description of the geometry for flow between eccentric rotating cylinders. The inner cylinder is rotated with angular velocity Ω, while the outer cylinder is kept stationary.

from a formal analysis of the method. In particular, we consider the flow between eccentric rotating cylinders, in the geometry shown in Fig. 4. The inner and outer cylinder are of radius R_i and R_o, respectively, with the distance between the cylinder centers given by e. The outer cylinder is kept at rest, while the inner cylinder is rotated at angular velocity Ω. For our purposes, we keep the geometry fixed, with $R_o/R_i = 2$, and the eccentricity $\varepsilon\ (= e/(R_o - R_i)) = 0.5$. The Reynolds number of the flow is defined as $R = R_i\Omega(R_o - R_i)/\nu$, where ν is the kinematic viscosity. Note this geometry could be conformally mapped to a concentric situation, and a

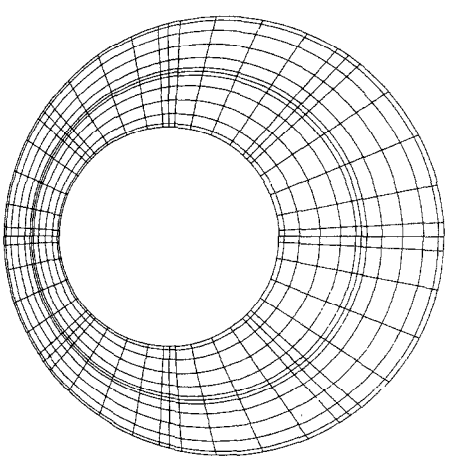

FIG. 5. The spectral element mesh used for solution of the Stokes and Navier–Stokes equations in the eccentric-cylinder geometry shown in Fig. 4. Two elements are used in the radial direction, and eight in azimuth.

Fourier/Chebyshev method (in azimuth, radius, respectively) used to solve the resulting equations. However, as a demonstration of our general isoparametric techniques, we leave the geometry in "primitive" form.

The eccentric-cylinder flow is a good test problem for numerical algorithms, in that complex flow phenomena (e.g., separation) occur at virtually all Reynolds numbers. Furthermore, for the case of steady Stokes flow ($R = 0$), the exact solution is known [22, 23]. We therefore begin by studying this particular case, skipping the

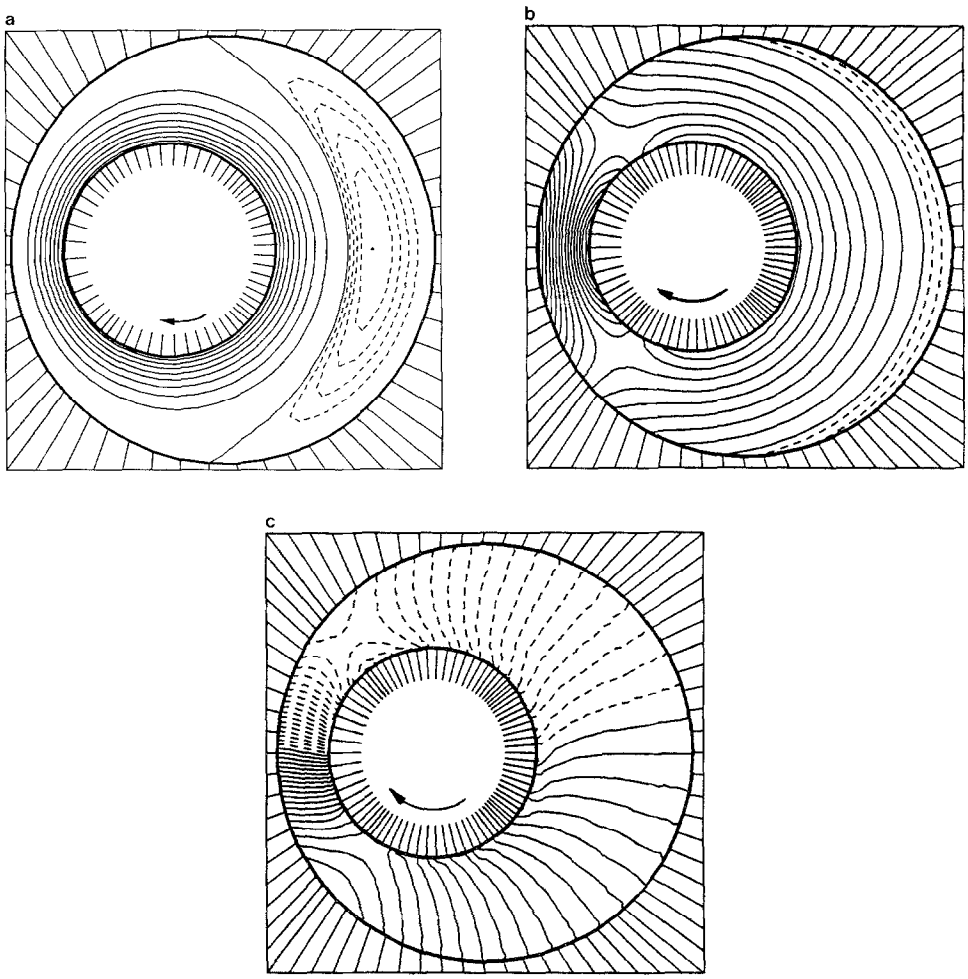

FIG. 6. Contours of the numerical solution for steamfunction (a), vorticity (b), and pressure (c) for steady Stokes flow in the eccentric-cylinder geometry. Continuous (dashed) lines represent constant positive (negative) function values with equal increments $\Delta_+(\Delta_-)$ between them. For the stream-function, $\psi_{max} = 0.307$, $\psi_{min} = -0.018$, $\Delta_+\psi = 0.0341$, $\Delta_-\psi = 0.00235$, for the vorticity $\omega_{max} = 3.019$, $\omega_{min} = -0.2202$, $\Delta_+\omega = 0.189$, $\Delta_-\omega = 0.0734$, and for the pressure $p_{max} = 4.761$, $p_{min} = -4.784$, $\Delta_+ p = 0.251$, $\Delta_- p = 0.239$.

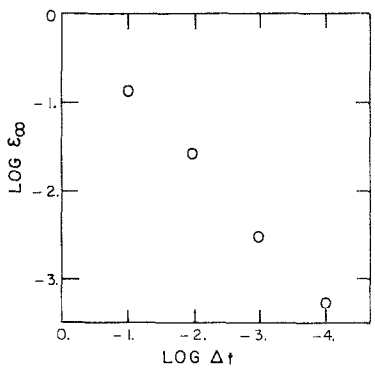

FIG. 7. Demonstration of the first-order error in time-step incurred by the Stokes solver. Here ε_∞ is the maximum error in the azimuthal velocity across the widest gap ($\theta = 0$). The mesh is sufficiently fine that spatial errors may be considered negligible.

non-linear contributions (33), and iterating our time-dependent Stokes solver (34)–(36) to a steady-state solution. In Fig. 5 we show the mesh used, with the order of the elements in the radial and azimuthal directions denoted N_r and N_θ, respectively. In Fig. 6 we show contours of the streamfunction, vorticity, and pressure, obtained with $N_r = N_\theta = 6$. As predicted by the analytical solution, we get (Stokes) separation occurring in the wide-gap region of the flow.

To demonstrate the $O(\Delta t)$ convergence of the splitting scheme, we plot in Fig. 7 the maximum error in the azimuthal velocity across the widest gap, $\varepsilon_\infty = \max_r |v_{\theta,\mathrm{ex}}(r, \theta = 0) - v_{\theta,\mathrm{num}}(r, \theta = 0)|$, as a function of Δt at fixed spatial resolution, $N_r = N_\theta = 6$. As predicted, the scheme is first order in time for the velocities. Note that although Fig. 7 does not prove that temporal errors are $O(\Delta t)$ for *time-dependent* flows, tests indicate that this is, in fact, the case.

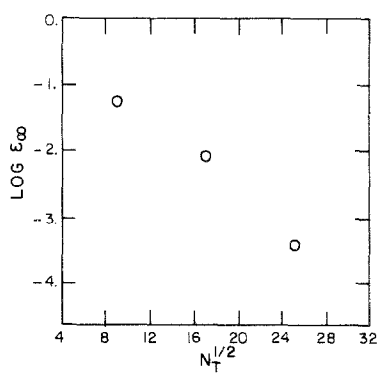

FIG. 8. Demonstration of the exponential convergence in space of the Stokes scheme. Here again ε_∞ is the maximum error in the azimuthal velocity across the widest gap ($\theta = 0$). The time-step is taken sufficiently small (10^{-4}) so that temporal errors may be considered negligible.

To demonstrate the exponential convergence of the solution in space, we plot in Fig. 8 ε_∞ as a function of $N_T^{1/2}$ (for fixed $\Delta t = 10^{-4}$), keeping $N_r = N_\theta$. With only 13 points (total) in the radial direction, the error is just slightly larger than 10^{-4}. Experimentation with meshes other than that shown in Fig. 5 indicates that the exponential convergence and good resolution properties presented here are not particularly sensitive to the details of the spectral element grid.

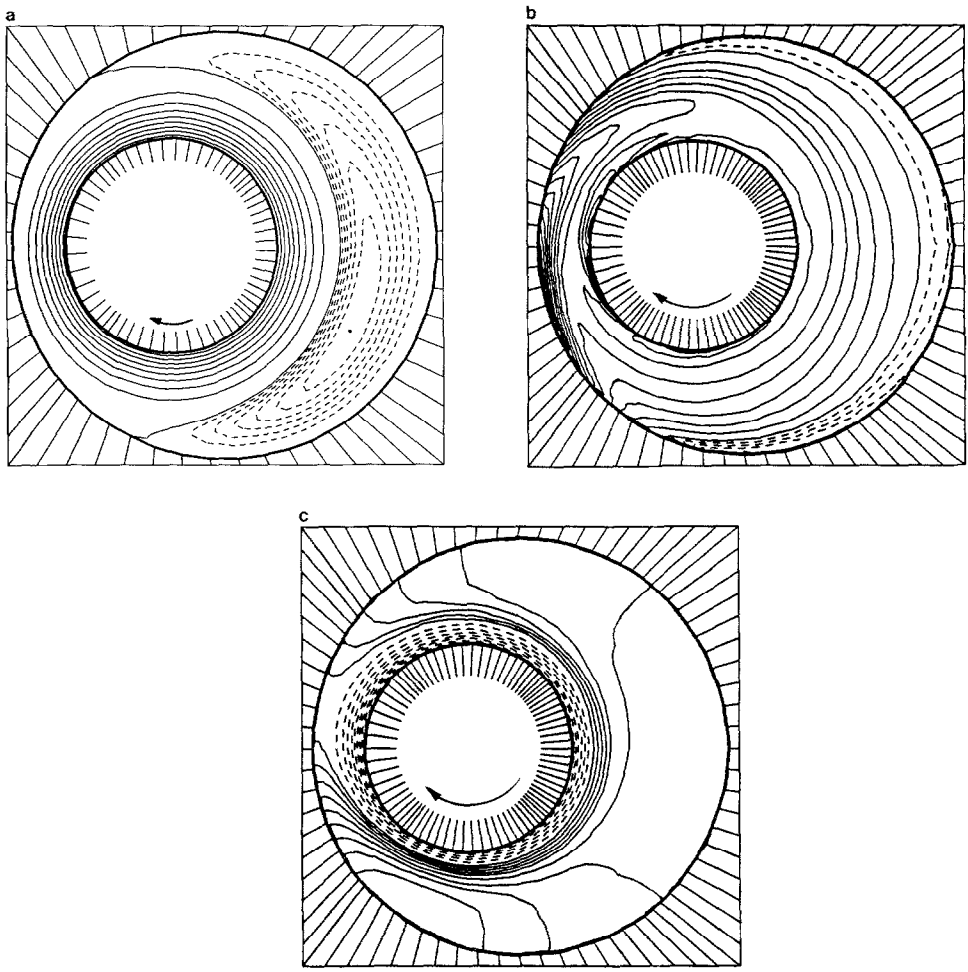

FIG. 9. Contours of the numerical solution for streamfunction (a), vorticity (b), and pressure (c) for steady flow in the eccentric-cylinder geometry at a Reynolds number of $R = 300$. Note the asymmetry in streamfunction and vorticity (as compared to Figs. 6a and b, respectively), the centrifugal effect in the pressure, and the shifting "downstream" of the center of the separated vortex. The plotting conventions are the same as in Fig. 6, however, now for the streamfunction, $\psi_{\max} = 0.290$, $\psi_{\min} = -0.0168$, $\Delta_+\psi = 0.0322$, $\Delta_-\psi = 0.00239$, for the vorticity $\omega_{\max} = 3.443$, $\omega_{\min} = -0.4735$, $\Delta_+\omega = 0.2025$, $\Delta_-\omega = 0.1184$, and for the pressure $p_{\max} = 0.06813$, $p_{\min} = -0.1702$, $\Delta_+ p = 0.00757$, $\Delta_- p = 0.02128$.

3.2. *Full Navier–Stokes Simulation*

The real application of the spectral element method is to direct integration of the full Navier–Stokes equations. Although an efficient and accurate Stokes solver is certainly a prerequisite for a successful Navier–Stokes simulation (hence our tests in Section 3.1), at large Reynolds number it is the treatment of the non-linear convective terms that is critical. It has been shown for both model problems [2, 5, 12], and Navier–Stokes calculations [6, 7], that the proposed (high-order collocation) scheme for the convective terms (33) results in minimal numerical dispersion and diffusion, and hence accurate resolution of unsteady phenomena in moderate-Reynolds-number flow.

As the difference in implementation for the explicit collocation terms in the rectilinear and general isoparametric formulations is relatively small, we do not repeat the test cases performed previously. Rather, we proceed directly to an example of solution of the full Navier–Stokes equations using the isoparametric spectral element method, namely simulation of the eccentric cylinder flow shown in Fig. 4 at a Reynolds number of $R = 300$. The mesh used is the same as that for Stokes flow (Fig. 5), with $N_r = N_\theta = 6$. The flow is found to reach a steady state, and the resulting streamlines, isobars, and vorticity contours are shown in Fig. 9. The flow is no longer symmetric about $y = 0$ (compare with the streamlines and vorticity in Figs. 6a and b, respectively), and the pressure (Fig. 9c) is seen to have a significant centrifugal component. Note also that the center of the separated vortex is shifted in the flow direction, as would be expected as inertial effects become important. Although there is no known exact solution for the eccentric cylinder flow when the Reynolds number is no longer small, our results indicate all the expected physical trends.

In summary, we have presented a high-order ("spectral") finite element technique for solution of the incompressible Navier–Stokes equations in complex geometry. The *generality* of the method derives from the (macro-) element spatial discretization; the *efficiency* is due to the use of collocation and (parallel) static condensation; the *accuracy* follows from the high-order interpolants used to represent the solution, data, and geometry. These attributes in no way depend on special properties of the geometry or flow (as is often the case for global spectral methods), and it would therefore appear that high-order methods do, in fact, constitute a viable approach for obtaining accurate solutions to general flow problems.

ACKNOWLEDGMENTS

We would like to thank Professors R. A. Brown and G. Strang, and Dr. M. Magen for helpful discussions. This work was supported by a Rockwell International Assistant Professorship (A.T.P.), by the NSF under Grant MEA-8212469, by the ONR, Contract N00014-84-C-0237, and by NASA Langley Research Center, Contract NAS1-16977. A large number of the computations were performed on a DEC VAX 750, supplied in part by a DEC External Research Program Grant.

REFERENCES

1. G. STRANG AND G. J. FIX, "An Analysis of the Finite Element Method," Prentice–Hall, Englewood Cliffs, N.J., 1973.
2. D. O. GOTTLIEB AND S. A. ORSZAG, "Numerical Analysis of Spectral Methods: Theory and Application," NSF–CBMS Monograph No. 26, SIAM, Philadelphia, 1977.
3. A. MCKERRELL, C. PHILLIPS, AND L. M. DELVES, *J. Comput. Phys.* **40** (1981), 444.
4. I. BABUSKA AND M. R. DORR, *Numer. Math.* **37** (1981), 257.
5. A. T. PATERA, *J. Comput. Phys.* **54** (1984), 468.
6. N. K. GHADDAR, A. T. PATERA, AND B. B. MIKIC, AIAA Paper No. 84-0495, 1984.
7. K. Z. KORCZAK AND A. T. PATERA, *in* "Proceedings, 9th Int. Conf. on Num. Methods in Fluid Dynamics," p. 314, Springer-Verlag, New York/Berlin, 1984.
8. K. Z. KORCZAK, Ph.D. thesis, Department of Mechanical Engineering, MIT, 1985.
9. L. M. DELVES AND C. PHILLIPS, *J. Inst. Math. Appl.* **25** (1980), 177.
10. L. ADAMS AND R. G. VOIGT, ICASE NASA Contractor Rep. No. 172219, 1983.
11. E. TADMOR, ICASE Rep. No. 84-40, 1984.
12. C. BASDEVANT, M. DEVILLE, P. HALDENWANG, J. M. LACROIX, P. ORLANDI, J. OUAZZINI, A. T. PATERA, AND R. PEYRET, *Computers and Fluids*, in press.
13. S. A. ORSZAG AND L. C. KELLS, *J. Fluid Mech.* **96** (1980), 159.
14. W. C. GEAR, "Numerical Initial Value Problems in Ordinary Differential Equations," Prentice–Hall, Englewood Cliffs, N.J., 1971.
15. S. A. ORSZAG, M. O. DEVILLE, AND M. ISRAELI, submitted for publication.
16. F. THOMASSET, "Implementation of Finite Element Methods for Navier–Stokes Equations," Springer-Verlag, New York/Berlin, 1981.
17. R. PEYRET AND T. D. TAYLOR, "Computational Methods for Fluid Flow," Springer-Verlag, New York/Berlin, 1983.
18. P. M. GRESHO, S. T. CHAN, R. L. LEE, AND C. D. UPSON, *Int. J. Numer. Methods Fluids* **4** (1984), 557.
19. R. L. SANI, P. M. GRESHO, R. L. LEE, AND D. F. GRIFFITHS, *Int. J. Numer. Methods Fluids* **1** (1981), 17.
20. J. DONEA, J. GIULIANI, K. MORGAN, L. QUARTAPELLE, *Int. J. Numer. Methods Eng.* **17** (1981), 790.
21. N. K. GHADDAR, G. E. KARNIADAKIS, AND A. T. PATERA, *Numerical Heat Transfer*, in press.
22. R. S. RIVLIN, *J. Non-Newtonian Fluid Mech.* **5** (1979), 79.
23. A. N. BERIS, R. C. ARMSTRONG, AND R. A. BROWN, *J. Non-Newtonian Fluid Mech.* in press.